

In Situ Dynamic Construction of a Copper Tin Sulfide Catalyst for High-Performance Electrochemical CO₂ Conversion to Formate

Ke Li, Jingwen Xu, Tingting Zheng, Yuan Yuan, Shuang Liu, Chunyue Shen, Taoli Jiang, Jifei Sun, Zaichun Liu, Yan Xu, Mingyan Chuai, Chuan Xia,* and Wei Chen*



Cite This: *ACS Catal.* 2022, 12, 9922–9932



Read Online

ACCESS |



Metrics & More



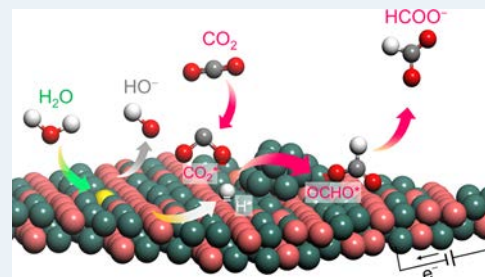
Article Recommendations



Supporting Information

ABSTRACT: Electrochemical reduction of CO₂ to produce fuels and chemicals is one of the most valuable approaches to achieve a carbon-neutral cycle. Recently, a diversity of catalysts have been developed to improve their intrinsic activity and efficiency. However, the dynamic evolution process and the *in situ* construction behavior of electrocatalysts under the working conditions are typically ignored. Here, we fully reveal the dynamic reduction process and phase transformation of a copper tin sulfide catalyst reconstructed by *in situ* reduction of the precatalyst Cu₂SnS₃ and CuS during electrochemical CO₂ reduction. Furthermore, the reconstructed catalyst reaches an outstanding electrochemical CO₂-to-formate conversion with a high Faradaic efficiency of 96.4% at an impressive production rate of 124889.9 μmol mg⁻¹ h⁻¹ under a partial current density of -241 mA cm⁻² (-669.4 A g⁻¹) in a flow-cell reactor. Theoretical calculations further demonstrate the strong charge interaction between the adsorbate and substrate to accelerate the charge transfer and decrease the formation energies of OCHO* and HCOOH* intermediates in the pathway of CO₂ to HCOOH, resulting in high selectivity for formate on the surface of the copper tin sulfide catalyst. This work paves the way for revealing the *in situ* dynamic process of the reconstructed catalyst and designing optimal catalysts with high catalytic activity and selectivity.

KEYWORDS: CO₂RR, dynamic construction, formate, copper–tin alloys, DFT



1. INTRODUCTION

The electrochemical conversion of carbon dioxide (CO₂) to carbon-based fuels and chemical feedstocks utilizing renewable electricity contributes to alleviating the current environmental problems of global warming and energy crisis and further reducing the growing emission of CO₂ to achieve a carbon-neutral cycle.^{1–5} Recently, considerable studies have been devoted to producing valuable products from the electrochemical CO₂ reduction reaction (CO₂RR).^{6–8} However, due to the multiple electron transfer reaction pathways of the CO₂RR, a diverse range of gaseous and liquid products ranging from C₁ to C₃ can be obtained during the process of the CO₂RR,^{9,10} such as carbon monoxide (CO),¹¹ methane (CH₄),¹² formic acid (HCOOH),¹³ ethylene (C₂H₄),¹⁴ ethanol (C₂H₅OH),¹⁵ and n-propanol (C₃H₈O).¹⁶ Among them, HCOOH has been considered as one of the most economical products, which can be used as a hydrogen energy carrier and chemical fuel.^{4,17} In addition, as a competitive transformational form with respect to traditional chemical engineering processes, the electrochemical conversion of CO₂ to formate (HCOO⁻) can be most likely industrialized owing to the high selectivity and activity.² To date, several metals have been reported to be able to achieve the selective electrochemical CO₂-to-formate conversion, such as indium (In),¹⁸ tin (Sn),¹⁹ bismuth (Bi),²⁰ and lead (Pb).⁵ However, these metal electrocatalysts generally show high overpotential, low activity (<200 mA cm⁻²), and poor

selectivity (<90%), suggesting the insufficient property to meet the large-scale industrial standards.

Recently, Sn-based catalysts have been attracting much attention in the electrochemical CO₂RR to formate, due to their low toxicity and earth abundance.^{21–25} However, the undistinguished catalytic activity still hinders their practical application for the CO₂RR. Thus, different strategies have been developed to promote their catalytic activities including overpotential, selectivity, and energy efficiency. For example, Zheng and co-workers developed a surface-lithium-doped Sn catalyst by electrochemical lithiation, which exhibited excellent electrocatalytic activity for the CO₂RR to formate with a Faradaic efficiency (FE) of 92%.²⁶ Tour and co-workers constructed a bimetallic CuSn-based catalyst through a re-lasing method for the CO₂RR toward formate with a FE of 99% at a partial current density of -26 mA cm⁻².²⁷ In addition, previous reports demonstrated that sulfur (S) can accelerate the electrochemical reduction of CO₂ to formate by enhancing the activation of H₂O and the formation of H* species on the surface

Received: May 31, 2022

Revised: July 11, 2022

Published: August 1, 2022



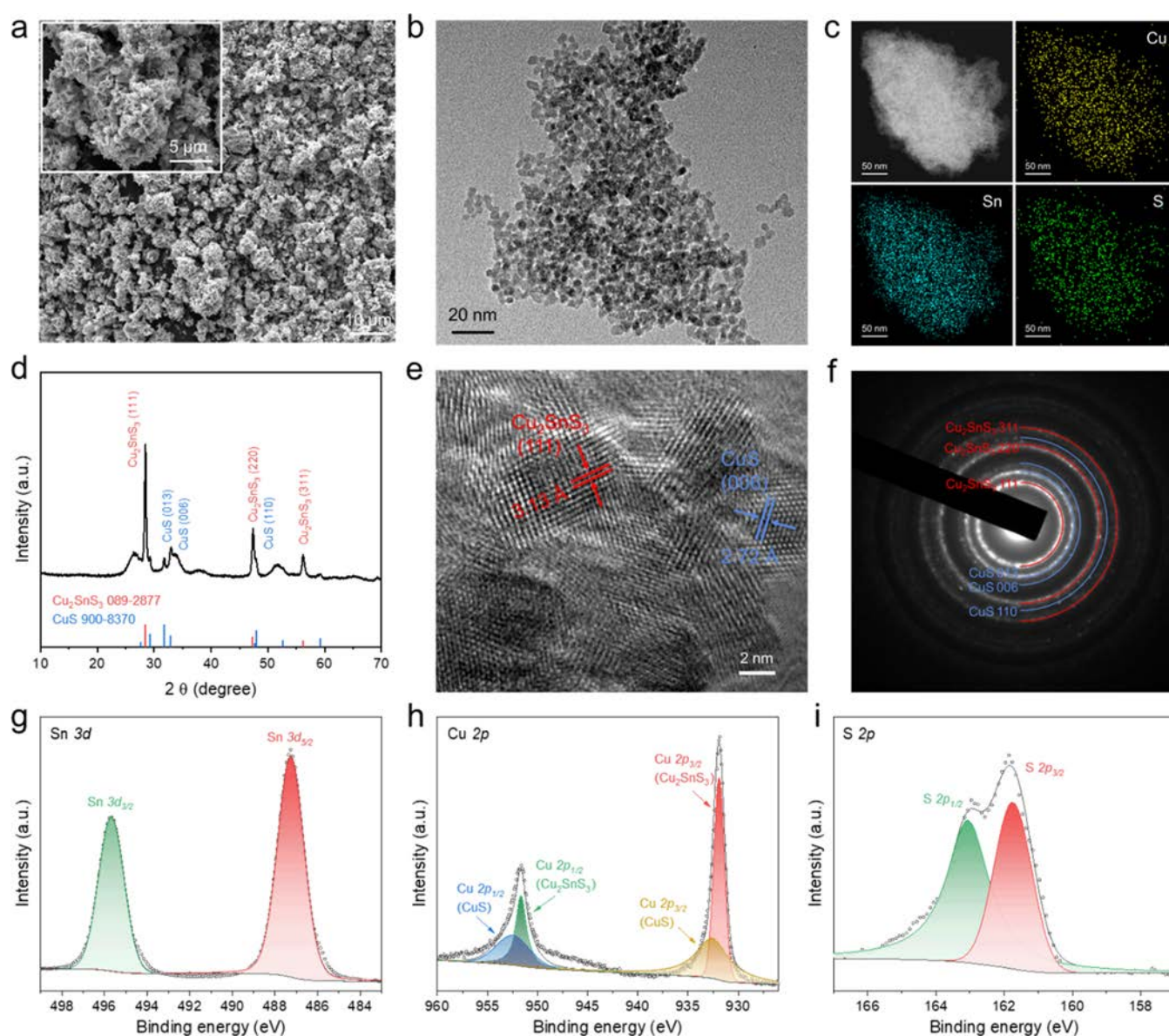


Figure 1. Structural characterizations of the precatalyst. (a) Scanning electron microscopy (SEM) image, (b) TEM image, (c) EDS elemental mapping, (d) XRD, (e) HRTEM, and (f) corresponding electron diffraction pattern of the precatalyst. (g) Sn 3d, (h) Cu 2p, and (i) S 2p XPS spectra of the precatalyst.

of the electrocatalyst.²⁸ For instance, tin-based sulfide (SnS) nanosheets achieved a maximum FE_{formate} of 88% with a current density of 120 mA cm^{-2} at -1.3 V vs reversible hydrogen electrode (RHE).²⁹ Furthermore, Sargent and co-workers demonstrated the effect of S for modulating the Sn catalyst on offering catalytic sites to improve the electrochemical CO_2RR to formate.³⁰ Therefore, it will be a great effective approach to employ the CuSn bimetallic alloy and S species in the CO_2RR system to increase catalytic sites, reduce the overpotential, and tune their electronic structures to further improve the electrocatalytic CO_2RR to formate.

Recent studies have paid much attention on regulating the catalytic activity and energy efficiency of catalysts for the CO_2RR . However, the morphological and structural evolutions were typically observed under the working conditions, which can further affect their catalytic performances.^{31–33} Specifically, the dynamic constructions of heterojunction,³⁴ phase transformation,³⁵ and single atom⁵ may occur during the electro-

chemical reduction of catalysts. Thus, it is of great significance to elaborate the dynamic evolution process and the *in situ* construction behavior of electrocatalysts under the working conditions, which would be helpful in understanding the catalytic reaction mechanisms.

In the work described herein, we investigate the *in situ* dynamic construction process of a copper tin sulfide (denoted as S-CuSn) catalyst via the electrochemical reduction of Cu_2SnS_3 and CuS compounds (denoted as a precatalyst) during the CO_2RR . The dynamic reduction process and phase transformation from the precatalyst to the resulting S-CuSn catalyst are fully revealed by *ex situ* X-ray diffraction (XRD), X-ray photoelectron spectroscopy (XPS), and transmission electron microscopy (TEM) characterizations. Additionally, the *in situ* reconstructed S-CuSn catalyst achieves outstanding catalytic activity for CO_2 -to-formate conversion at a wide potential range. It shows a maximum conversion efficiency of 91.5% for formate with a partial current density (j_{formate}) of about -54.9 mA cm^{-2}

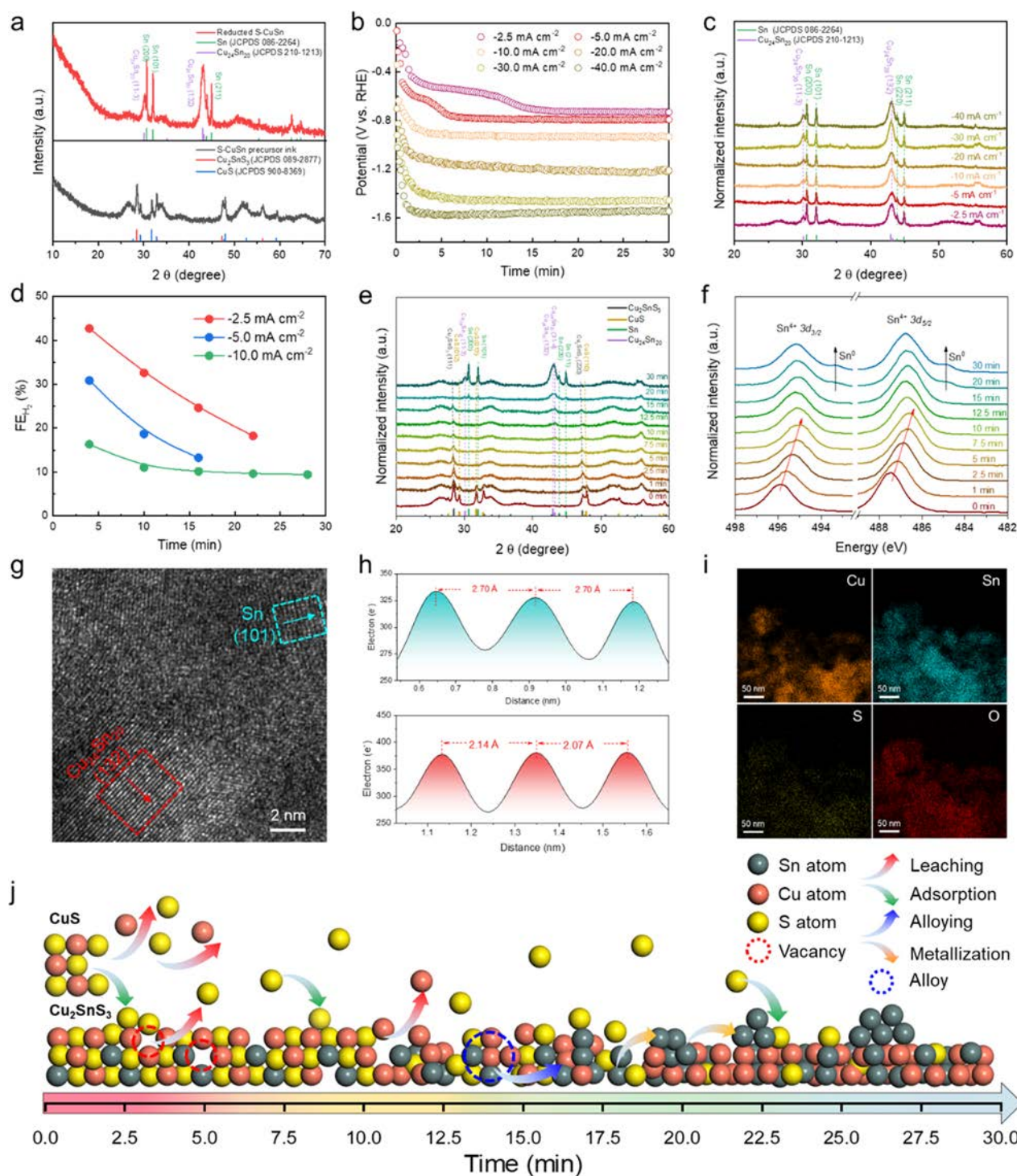


Figure 2. *In situ* construction mechanism of the S-CuSn catalyst. (a) XRD patterns of the precatalyst, collected before and after *in situ* reduction at a current density of -2.5 mA cm^{-2} in a CO_2 -saturated 0.5 M KHCO_3 electrolyte for 12 h. (b) V vs t curves of the precatalyst in a CO_2 -saturated 0.5 M KHCO_3 electrolyte at current densities of -2.5 , -5 , -10 , -20 , -30 , and -40 mA cm^{-2} . (c) XRD patterns of the precatalyst, collected after *in situ* reduction at -2.5 , -5 , -10 , -20 , -30 , and -40 mA cm^{-2} in a CO_2 -saturated 0.5 M KHCO_3 electrolyte for 0.5 h. (d) Corresponding FEs of H_2 on the precatalyst at current densities of -2.5 , -5 , and -10 mA cm^{-2} . (e) XRD patterns of the precatalyst, collected after *in situ* reduction at -2.5 mA cm^{-2} for different durations in a CO_2 -saturated 0.5 M KHCO_3 electrolyte. (f) Corresponding Sn 3d spectra of the precatalyst, collected after *in situ* reduction at -2.5 mA cm^{-2} for different durations in a CO_2 -saturated 0.5 M KHCO_3 electrolyte. (g) HRTEM, (h) partial enlarged line intensity profiles acquired in (g) highlighted with cyan and red boxes, and (i) EDS elemental mapping of the precatalyst, collected after *in situ* reduction at -2.5 mA cm^{-2} in a CO_2 -saturated 0.5 M KHCO_3 electrolyte for 0.5 h. (j) Schematic diagram of the *in situ* dynamic construction process of the S-CuSn catalyst.

(-109.8 A g^{-1}) at -1.20 V vs RHE in a traditional H-cell reactor. In a standard flow-cell device, the S-CuSn catalyst exhibits a maximal FE of 96.4% for formate with a j_{formate} of -241.0 mA

cm^{-2} (-669.4 A g^{-1}) at -2.22 V vs RHE , and the corresponding formate production rates can reach as high as $124889.9 \mu\text{mol mg}^{-1} \text{ h}^{-1}$. Moreover, density functional theory (DFT)

calculations reveal that the excellent formate selectivity can be attributed to the strong electron interaction between the adsorbate and the surface of S-CuSn. This work provides a general strategy to investigate the dynamic construction of electrocatalysts under the operating conditions and probe the actual active sites of the working catalysts.

2. RESULTS AND DISCUSSION

2.1. Synthesis and Characterization of Precatalysts.

The precatalyst, a compound of Cu_2SnS_3 and CuS , was synthesized by a hydrothermal method with the reaction of $\text{CuCl}_2 \cdot 2\text{H}_2\text{O}$, $\text{SnCl}_4 \cdot 2\text{H}_2\text{O}$, and $\text{CH}_4\text{N}_2\text{S}$ in deionized (DI) water at a temperature of 210 °C for 7.5 h (for details of the “synthesis of the precatalyst” scheme, see the Methods). Figure 1a shows that the precatalyst has a morphology of microflowers, which consist of small nanoparticles (Figure 1b). Energy-dispersive X-ray spectroscopy (EDS) elemental mapping clearly exhibits the coexistence and uniform dispersion of Cu, Sn, and S atoms in the precatalyst, suggesting the successful preparation of the precatalyst (Figure 1c). Figure 1d shows the powder X-ray diffraction (XRD) patterns of the precatalyst, which exhibits the main characteristic peaks of the (111), (220), and (311) planes of Cu_2SnS_3 and (013), (006), and (110) planes of CuS . High-resolution transmission electron microscopy (HRTEM) demonstrates the clear lattice spacings of 3.13 and 2.72 Å, which correspond to the (111) and (006) planes of Cu_2SnS_3 and CuS , respectively. The results further indicate the coexistence of Cu_2SnS_3 and CuS in the precatalyst. The selected area electron diffraction (SAED) pattern reveals the form of Cu_2SnS_3 (JCPDS 089-2877) and CuS (JCPDS 900-8369) with obvious lattice spacing, which is in good agreement with the lattice fringes (Figure 1e,f). The X-ray photoelectron spectroscopy (XPS) survey spectra clearly reveal the presence of Sn, Cu, and S elements in the precatalyst (Figure S1 and Table S1, Supporting Information). The high-resolution XPS spectra of Sn 3d for the precatalyst show two characteristic peaks at the binding energy of 495.7 and 487.3 eV with a separation of 8.4 eV (Figure 1g), which can be assigned to Sn 3d_{3/2} and Sn 3d_{5/2}, respectively,^{36–38} suggesting the Sn^{4+} state in the precatalyst. The Cu 2p spectrum exhibits four obvious peaks of Cu 2p_{1/2} (951.7, 952.5 eV) and Cu 2p_{3/2} (931.8, 932.6 eV) with a separation of 19.9 eV, indicating the +2 and +1 oxidation states of Cu species for Cu_2SnS_3 and CuS in the precatalyst, respectively (Figure 1h).^{36,38–40} The high-resolution S 2p spectrum can be deconvoluted into two components, corresponding to S 2p_{1/2} (163.1 eV) and S 2p_{3/2} (161.7 eV) (Figure 1i).^{6,7,36} Additionally, the elemental ratio of the precatalyst was also investigated by ICP-MS characterization, in which the atomic ratios of Cu/Sn and S/Sn are close to 2 and 3, respectively. (Figure S2, Supporting Information). The results of TEM, XRD, XPS, and ICP further confirm the successful synthesis of the precatalyst.

2.2. In Situ Dynamic Construction of the S-CuSn catalyst. To better understand and reveal the changes of the chemical composition and structure of the electrocatalyst under electrochemical CO_2RR conditions, the *in situ* dynamic reconstruction process of the S-CuSn catalyst was fully explicated. The precatalyst was first tested as an electrocatalyst in a CO_2 -saturated 0.5 M KHCO_3 aqueous solution (pH = 7.4) under different current densities or durations. Figure 2a shows the XRD pattern of the tested precatalyst collected after *in situ* reduction at a current density of -2.5 mA cm^{-2} for 12 h, indicating the formation of the $\text{Cu}_{24}\text{Sn}_{20}$ (JCPDS 210-1213) alloy and Sn (JCPDS 086-2264) metal during the reconstruction

process. To further estimate the constructed structure of the S-CuSn catalyst, different current densities were applied for 30 min under the working conditions. Figure 2b exhibits the V vs t curves of the precatalyst tested at current densities of -2.5 , -5 , -10 , -20 , -30 , and -40 mA cm^{-2} . Specifically, several electrochemical platforms were obviously observed from the voltage curves, suggesting that various forms existed in the reconstruction process. Moreover, the corresponding phase structures of the S-CuSn catalyst *in situ* reduced in the electrolyte with different current densities are presented in Figure 2c. Some pronounced characteristic peaks of the $\text{Cu}_{24}\text{Sn}_{20}$ alloy and Sn metal were significantly formed and further revealed the stability of the reconstructed structures after the *in situ* reduction. Furthermore, the corresponding high-resolution Sn 3d spectra display the representative peaks of Sn^{4+} (including 3d_{3/2} and 3d_{5/2}) and Sn^0 (Figure S3, Supporting Information), suggesting the existence of Sn oxide and metallic Sn. Notably, the surface of the S-CuSn catalyst is subjected to oxidation when exposed to air, which leads to the formation of the Sn^{4+} state.⁴¹ The high-resolution Cu 2p spectra of the S-CuSn catalyst *in situ* reduced with different current densities exhibit all typical characteristic peaks, and the X-ray excited Auger spectroscopy (XEAS) for Cu LMM indicated that the surface of the reconstructed S-CuSn may be oxidized in the air (Figures S4 and S5). The S 2p spectra of the S-CuSn catalyst *in situ* reduced with different current densities exhibit all typical characteristic peaks (Figure S6, Supporting Information). However, to further demonstrate the effect of the reconstruction process of S-CuSn catalyst on the electrochemical conversion of CO_2 , online electrochemical gas chromatography tests were carried out. As shown in Figure 2d, the FEs of the gas product (H_2) from CO_2 conversion gradually reduced during the *in situ* dynamic construction progress. Additionally, the FEs of H_2 in the first 30 min under a current density of -2.5 mA cm^{-2} were higher than those with a larger current density. This phenomenon, which is in good agreement with the V vs t curves (Figure 2b), can be mainly attributed to the slow reconstruction process of the S-CuSn catalyst and the transition of multiphase structures.⁴² Therefore, to deeply elaborate on the dynamic construction process of the $\text{Cu}_{24}\text{Sn}_{20}$ alloy and Sn metal from the precatalyst, we also investigated the phase transformation of the precatalyst *in situ* reduced at -2.5 mA cm^{-2} in the first 30 min through *ex situ* XRD. The dynamic construction process of the formation of the $\text{Cu}_{24}\text{Sn}_{20}$ alloy and Sn metal from the precatalyst is clearly revealed in Figure 2e. Specifically, the characteristic peaks of Cu_2SnS_3 and CuS were obviously observed before the *in situ* reduction (0 min), while the CuS gradually disappeared and was reduced to Cu and dissolved in the electrolyte after the *in situ* reduction for 2.5 min. The results of ICP further proved that Cu ($0.33 \mu\text{g mL}^{-1}$) was detected in the electrolyte. With the reduction time increased to 10 min, Cu_2SnS_3 was also gradually reduced, and the diffraction peaks have been evidently shifted in a low-angle region, which can be attributed to the leaching of S from Cu_2SnS_3 and the formation of S vacancies in Cu_2SnS_3 .^{16,43,44} Furthermore, the $\text{Cu}_{24}\text{Sn}_{20}$ alloy and Sn metal consecutively emerged after the *in situ* reduction for 12.5 and 20 min, respectively. Afterward, Cu_2SnS_3 was completely reduced, and the reconstructed structure tended to be stable.

Furthermore, the elemental compositions and chemical states of the corresponding reconstructed structures were investigated by XPS measurements. Figure 2f exhibits the high-resolution Sn 3d spectra of the precatalyst *in situ* reduced at -2.5 mA cm^{-2} in

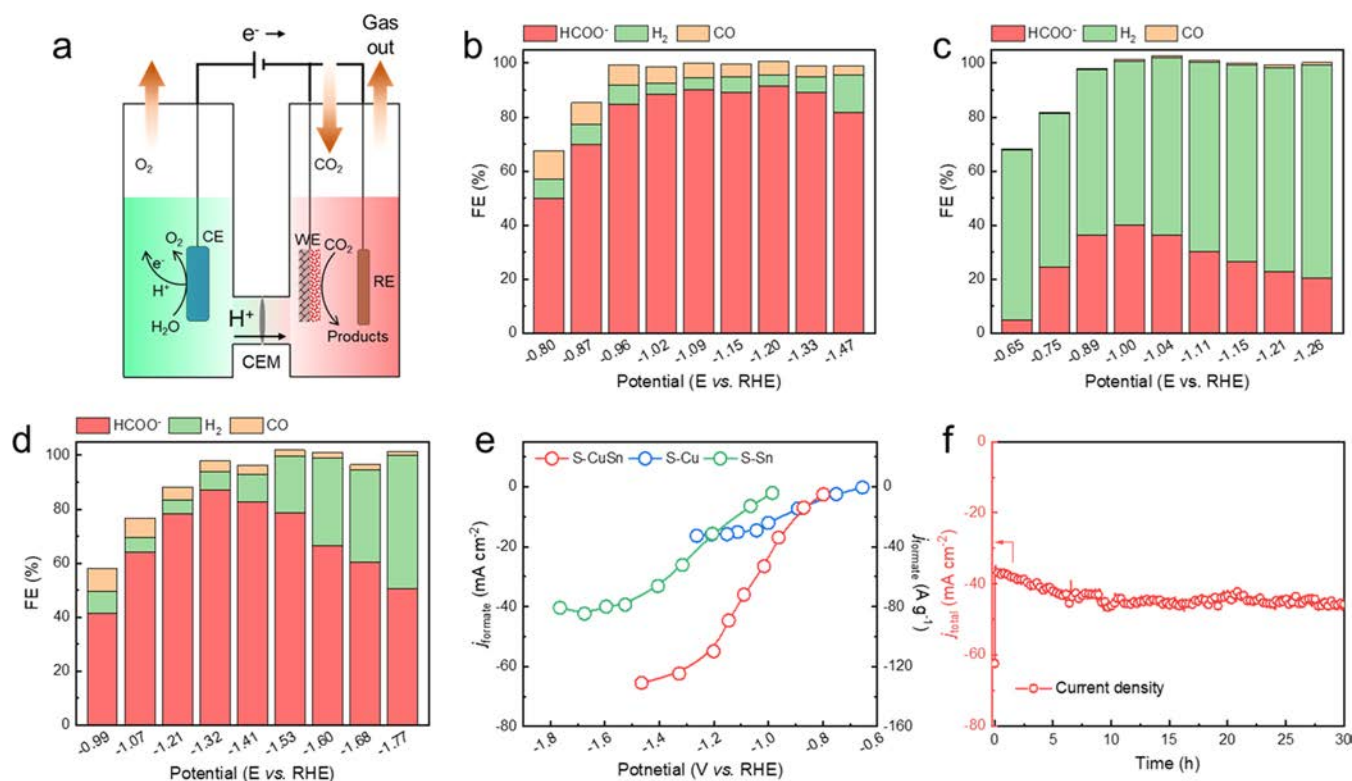


Figure 3. Electrocatalytic CO_2 reduction to formate using the S-CuSn catalyst in a H-type reactor. (a) Schematic diagram of a H-type reactor for the electrochemical CO_2 RR to formate. (b–d) FEs of each CO_2 reduction products by S-CuSn (b), S-Cu (c), and S-Sn (d) catalysts at different potentials. (e) Partial current densities of formate on S-CuSn, S-Cu, and S-Sn catalysts at different potentials. (f) Chronoamperometric stability test at -1.05 V vs RHE for 30 h, which indicates an average liquid product FE of about 85%.

the first 30 min, significantly manifesting that the binding energy of Sn^{4+} shifted to a lower energy and the formation of Sn^0 , which is mainly attributed to the alloying and metallization of Sn^{4+} under the *in situ* reconstruction process.^{6,34,45} Furthermore, to further reveal the phenomenon of the high proportion of Sn^{4+} , XPS characterization with Ar plasma etching was applied to the catalyst. As shown in Figure S7, the atomic content of Sn^0 species on the reconstructed S-CuSn catalyst has been significantly enhanced after Ar plasma etching, and the corresponding atomic contents of Sn^0 and Sn^{4+} are calculated to be ca. 37.7 and 62.3%, respectively. Therefore, we deem that the high proportion of Sn^{4+} in the reconstructed S-CuSn catalyst can be mainly derived from the surface oxidation of the nanosized tin particles.⁶ The Cu 2p and S 2p spectra further confirm the existence of Cu and S elements and the phase transformations of the precatalyst *in situ* reduced at -2.5 mA cm^{-2} in the first 30 min (Figures S8 and S9, Supporting Information). Specifically, comparison of the S 2p XPS spectra before and after reconstruction reveals that the S atoms were significantly removed (Figure S10a), and the S 2p spectrum of the reconstructed S-CuSn shows two characteristic peaks located at 163.3 and 162.0 eV, which can be assigned to S 2p_{1/2} and S 2p_{3/2}, respectively (Figure S10b). Additionally, the content of the S element was significantly decreased with the increase of the reduction time, and the decrease of S in the catalyst is also agreed well with the increased S amount ($5.9\text{ }\mu\text{g mL}^{-1}$) in the electrolyte based on the ICP characterization (Table S2, Supporting Information), suggesting that the S elements were leached during the *in situ* reconstruction process, which is further consistent with the shifted diffraction peaks of Cu_2SnS_3 (Figure 2e).^{6,28} The corresponding ratios of Sn, Cu,

and S elements in different reconstruction processes were compared to further reveal the phase transformations of the precatalyst (Figure S11 and Table S2, Supporting Information). Combined with the results of *ex situ* XRD of the precatalyst *in situ* reduced at -2.5 mA cm^{-2} for different durations, firstly, the ratios of Sn and S increased, and the Cu content decreased owing to the complete reduction of CuS . Then, the leaching of S from Cu–S bonds in Cu_2SnS_3 increased the contents of Sn and Cu. Furthermore, the reduced Cu from Cu^+ in Cu_2SnS_3 resulted in the decrease of Cu and increase of Sn and S. With the further leaching of S from Sn–S bonds in Cu_2SnS_3 and the formation of Sn metal, the contents of Sn and Cu increased and that of S decreased. Finally, the ratios of Sn, Cu, and S were barely changed due to the stability of the final reconstructed structure. The atomic ratio of Cu to Sn further demonstrated the above-mentioned reconstruction processes (Figure S12).

To further demonstrate the phase transformation and stability of the reconstructed structure, the precatalyst *in situ* reduced at -2.5 mA cm^{-2} for 30 min was investigated by TEM characterization. The reconstructed structure maintained nanosized morphology after *in situ* reduction (Figure S13, Supporting Information). The HRTEM image and the corresponding line intensity profiles also show clear lattice spacings of the (132) plane of $\text{Cu}_{24}\text{Sn}_{20}$ and (101) plane of Sn, further indicating the formation of $\text{Cu}_{24}\text{Sn}_{20}$ alloy and Sn metal after the *in situ* reconstruction of the precatalyst (Figures 2g,h and S14, Supporting Information). The HRTEM image shows the clear lattice spacings of the (132) plane of $\text{Cu}_{24}\text{Sn}_{20}$, further indicating the formation of the $\text{Cu}_{24}\text{Sn}_{20}$ alloy in the reconstructed S-CuSn catalyst. (Figure S15, Supporting Information). STEM-EDS elemental mapping images exhibit a homogeneous distribution

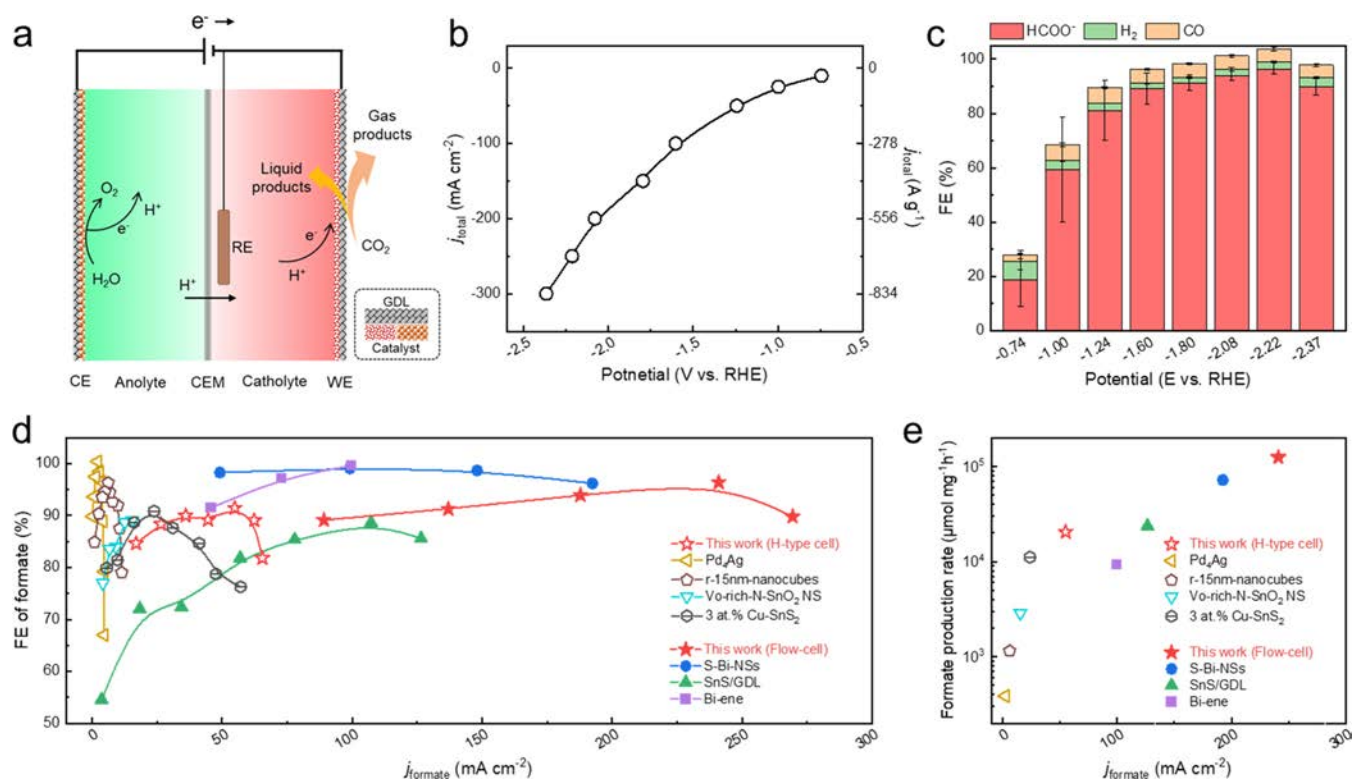


Figure 4. Electrochemical CO₂-to-formate conversion on the S-CuSn catalyst in a flow-cell reactor. (a) Schematic diagram of a flow-cell reactor for the electrochemical reduction of CO₂ to formate. (b) Overall current density of the S-CuSn catalyst on a GDL in a flow-cell system. (c) Corresponding FEs of the resultant reduction products. (d, e) Comparisons of (d) FEs and (e) formate production rates with respect to the formate partial current densities for our S-CuSn catalyst with various catalysts reported.

of Sn, Cu, S, and O atoms (Figure 2i). Based on the analysis of the high-resolution O 1s spectrum, the O element in the reconstructed S-CuSn might be derived from the adsorption and oxidation of the reconstructed S-CuSn catalyst in air (Figure S16, Supporting Information). Based on the results of *ex situ* XRD, XPS, and HRTEM of the precatalyst *in situ* reduced under the working conditions with different current densities or durations, a schematic diagram of the *in situ* dynamic reconstructed S-CuSn catalyst is summarized and presented in Figures 2j and S17 (Supporting Information), whose overall process can be divided into five stages: (A) the reduction of CuS, (B) the leaching of S from Cu₂SnS₃, (C) the formation of Cu₂₄Sn₂₀ alloys, (D) the formation of Sn metal, and (E) the stable structure of S/Sn co-doped Cu₂₄Sn₂₀ alloys.

2.3. Electrochemical Performance of the CO₂RR.

Inspired by the unique constructed S-CuSn catalyst, its CO₂RR activity was firstly estimated in a standard H-type reactor using CO₂-saturated 0.5 M KHCO₃ as an electrolyte (Figures 3a and S18, details in the Methods, Supporting Information). The gas and liquid products from CO₂ conversion were separately analyzed by online gas chromatography (GC) and offline nuclear magnetic resonance (NMR) spectroscopy, respectively. The linear sweep voltammetry (LSV) of the S-CuSn catalyst shows that the cathodic current density increased steadily and reached about -100 mA cm⁻² at -1.55 V vs RHE in the CO₂-saturated electrolyte compared to that under an Ar atmosphere, suggesting that the CO₂ molecules participate in the reaction with excellent electrochemical activity of CO₂ conversion (Figure S19). Particularly, the S-CuSn catalyst exhibits extraordinary performance for the CO₂RR to formate in the H-type cell. The maximal FE of formate reaches about

91.5% with a partial current density (j_{formate}) of about -54.9 mA cm⁻² (-109.8 A g⁻¹) at -1.20 V vs RHE (Figures 3b and S20). The corresponding formate production rate reaches 20484.0 μmol mg⁻¹ h⁻¹, indicating the high catalytic activity of the *in situ* reconstructed S-CuSn catalyst for CO₂-to-formate conversion. In addition, the S-CuSn catalyst exhibits impressive FEs of formate (>80%) at a wide potential range from -0.96 to -1.47 V vs RHE, and the corresponding j_{formate} range from -16.9 to -65.4 mA cm⁻². To highlight the excellent selectivity of the S-CuSn catalyst, two control catalysts were prepared, i.e., CuS and SnS₂ (denoted as S-Cu and S-Sn). The corresponding structural characterizations are shown in Figures S21 and S22 (Supporting Information). The control catalysts show small differences of LSV curves in CO₂- and Ar-saturated electrolytes compared to that of the reconstructed S-CuSn catalyst (Figure S23, Supporting Information). Moreover, the S-Cu catalyst displays low electrochemical activity of CO₂ conversion to formate and high activity of the HER, where the corresponding FE of H₂ exceeds 60% at a potential range from -0.65 to -1.26 V vs RHE (Figure 3c). Although the S-Sn catalyst exhibits a high FE of formate of about 87% at -1.32 V vs RHE with a j_{formate} of -26.1 mA cm⁻² (-52.2 A g⁻¹), such performance is inferior to that of the S-CuSn catalyst (Figure 3d). Overall, the S-CuSn catalyst exhibits a higher j_{formate} (91.5%) than those of CuS and SnS₂ catalysts (Figure 3e), suggesting that it has a high energy efficiency (52.7%) and low overpotential (-1.03 V) during the CO₂RR to formate. These comparisons further highlight the vital role of the *in situ* reconstructed S-CuSn in the electrochemical CO₂-to-formate conversion. The S-CuSn catalyst can also continuously and stably perform at a constant potential of -1.05 V vs RHE with a current density of about -45 mA cm⁻²

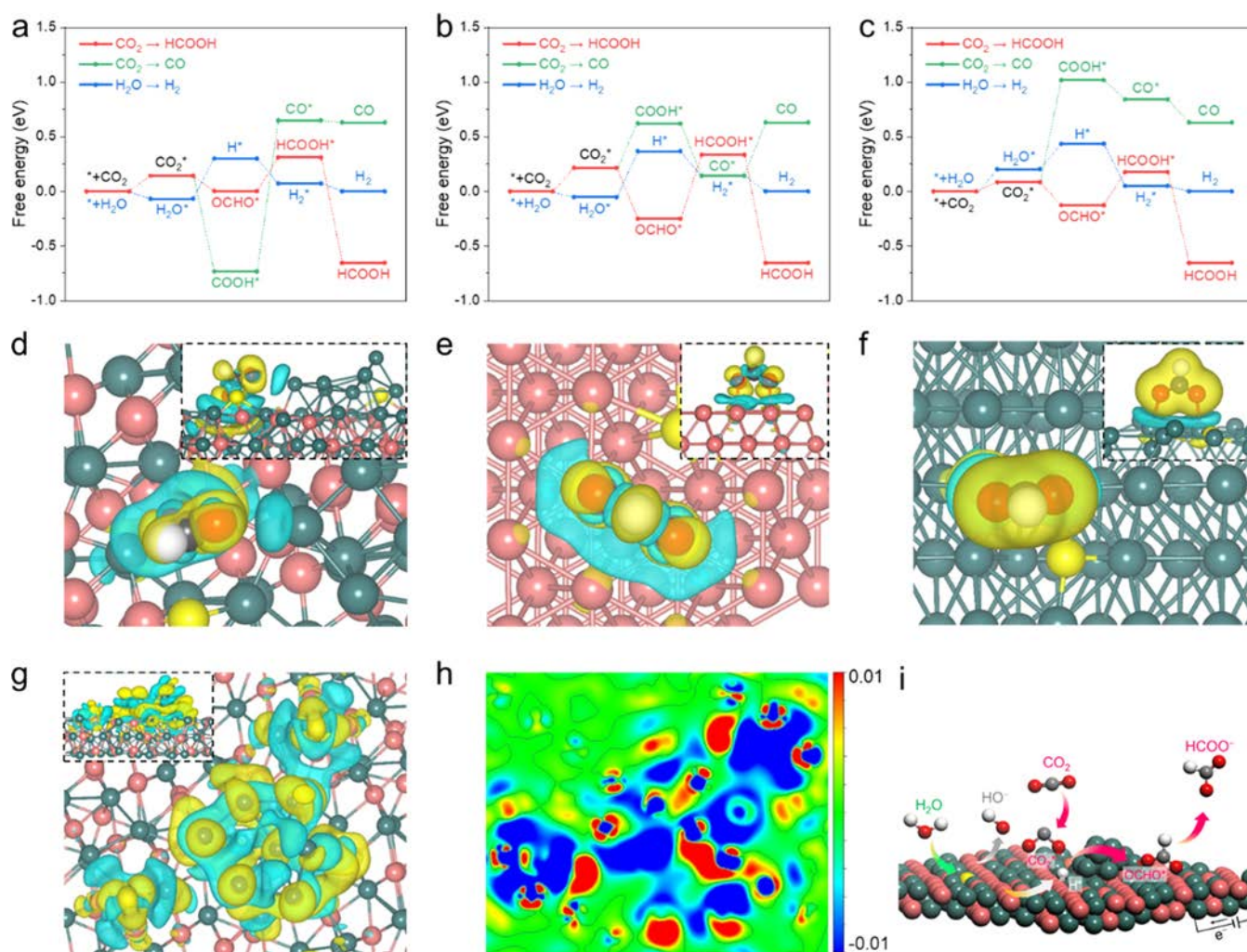


Figure 5. Theoretical calculations and reaction scheme. (a–c) Gibbs free energy diagrams for the pathways of CO_2 -to- HCOOH , CO_2 -to- HCOOH , and H_2O -to- H_2 conversions on S-CuSn (a), S-Cu (b), and S-Sn (c). (d–f) Differential charge density distributions of OCHO^* adsorbed on S-CuSn (d), S-Cu (e), and S-Sn (f). Yellow and cyan isosurfaces show the electron accumulation and depletion, respectively. Isosurface value = $0.008 \text{ e } \text{\AA}^{-3}$. (g, h) Differential charge density distribution of the S-CuSn interface (g) and the corresponding sliced 2D contour map with a Z value of 4.93 \AA (h). Isosurface value = $0.01 \text{ e } \text{\AA}^{-3}$. (i) Schematic illustration for the proposed electrochemical CO_2RR mechanism over S-CuSn. The green, bronze, yellow, red, gray, and white balls represent Sn, Cu, S, O, C, and H atoms, respectively.

for 30 h, and the total FEs of CO and H_2 are about 15% (Figure 3f). The XRD and TEM characterizations of the S-CuSn catalyst after a long-term stability test were also carried out (Figures S24 and S25, Supporting Information), revealing that the nanosized and reconstructed structure is well-preserved and explaining the prominent electrochemical activity of CO_2 conversion to formate. However, there are still a small number of nanoparticles, which were formed after the CO_2RR , would slightly increase the FE of H_2 .

Furthermore, we evaluated the CO_2RR property of the S-CuSn catalyst assembled on a gas diffusion layer (GDL) in a three-electrode flow-cell reactor using a 0.5 M KHCO_3 electrolyte (Figures 4a and S26, details in the Methods, Supporting Information). The S-CuSn catalyst reaches a maximal FE of 96.4% for formate with a j_{formate} of $-241.0 \text{ mA cm}^{-2}$ (-669.4 A g^{-1}) at -2.22 V vs RHE (Figure 4b,c). In particular, the S-CuSn catalyst achieves the highest j_{formate} of $-269.4 \text{ mA cm}^{-2}$ with a specific activity of -748.3 A g^{-1} for CO_2 conversion to formate, suggesting the excellent activity efficiency of the *in situ* reconstructed copper tin sulfide catalyst. Compared with the recently reported literature, the *in situ* reconstructed S-

CuSn catalyst exhibits impressive selectivity and j_{formate} for the electrochemical CO_2 -to-formate conversion (Figure 4d and Table S3, Supporting Information).^{6,7,46–50} Encouragingly, the corresponding formate production rates can reach 20484.0 and $124889.9 \text{ } \mu\text{mol mg}^{-1} \text{ h}^{-1}$ in H-type and flow-cell reactors, respectively, suggesting the outstanding yields among all the reported CO_2 -to-formate reduction catalysts (Figure 4e and Table S3, Supporting Information).

2.4. Theoretical Calculations of the Catalytic Mechanism. To further reveal the catalytic mechanism of the excellent electrochemical performance for CO_2 -to-formate conversion on the *in situ* reconstructed S-CuSn catalyst, we performed theoretical calculations of three types of models, including S/Sn-co-doped CuSn alloy, S-doped Cu, and S-doped Sn (respectively, denoted as S-CuSn, S-Cu, and S-Sn) (Figure S27, details in the Methods, Supporting Information). We calculated the Gibbs free energies for the formation of HCOOH and CO from CO_2 and the formation of H_2 from H_2O . Specifically, for the formation of HCOOH, two proton/electron transfer steps participate in the electrochemical CO_2 conversion to HCOOH, including the protonation of CO_2 to the OCHO^*

intermediate and the transformation of the OCHO^* intermediate to the HCOOH^* intermediate ($* + \text{CO}_2 + \text{H}^+ + \text{e}^- \Rightarrow \text{OCHO}^*$; $\text{OCHO}^* + \text{H}^+ + \text{e}^- \Rightarrow \text{HCOOH}^*$).^{51,52} Then, the formed HCOOH^* intermediate would desorb from the surface of the catalyst and accelerate the formation of HCOOH . In addition, the adsorption of the OCHO^* intermediate is regarded as the determining step for the process of electrochemical CO_2 conversion to HCOOH .^{6,8} The formation of CO from electrochemical CO_2 is also a two-proton/electron transfer steps process.⁵³ Specifically, it includes the protonation of CO_2 to the COOH^* intermediate, which is believed to be the intermediate for the formation of CO ,⁵⁴ the dihydroxylation of the COOH^* intermediate to the adsorbed CO^* intermediate, and the separation of the CO^* intermediate from the surface of the catalyst.⁵⁵ The competing HER, which occurs by a bound H^* intermediate,⁵⁶ can also react on the catalyst during the CO_2RR and would significantly affect the conversion efficiency of HCOOH . Therefore, the Gibbs free energies for the CO_2RR to HCOOH and CO as well as H_2O to H_2 on the surfaces of S-CuSn, S-Cu, and S-Sn have been calculated, and the corresponding results are concluded in Table S4–S7 (Supporting Information).

On the surface of S-CuSn, firstly, the CO_2 molecule needs to be activated, and the corresponding Gibbs free energy for the formation of CO_2^* is 0.14 eV. Then, the CO_2^* captures a proton/electron pair or the adsorbed H intermediate to form OCHO^* with a free energy of -0.14 eV, indicating that the HOCO^* can be spontaneously formed in thermodynamics from CO_2^* on the surface of S-CuSn (Figures 5a and S28a, Supporting Information). However, the Gibbs free energy for the formation of HCOOH^* is 0.31 eV, which is higher than that of CO_2^* and OCHO^* and the desorption of HCOOH^* (-0.97 eV) to produce HCOOH , suggesting that the formation of HCOOH^* from OCHO^* is the potential-limiting step for the CO_2 -to- HCOOH conversion on the surface of S-CuSn. Additionally, the formation of CO from CO_2 and H_2 from H_2O can also happen during the CO_2RR (Figure S28b,c, Supporting Information). Based on the DFT calculations, the potential-limiting steps for the pathways of CO and H_2 are determined to be the formations of CO^* and H^* , respectively. The corresponding Gibbs free energies for the formations of CO^* and H^* are 1.38 and 0.37 eV on the surface of S-CuSn, respectively (Figure 5a). The results manifest that the energy barrier of the potential-limiting step for CO_2 -to- HCOOH conversion is lower than that of the pathways of CO and H_2 , indicating that the pathway of HCOOH is more energy-favorable on the surface of S-CuSn. It also interprets the experimentally high activity and efficiency of HCOOH for the S-CuSn catalyst during the CO_2RR . As a comparison, the same calculations were also conducted on the models of S-Cu and S-Sn. For the structure of S-Cu, the potential-limiting step for the formation of H^* from the active H_2O (H_2O^*) is lower than the potential-limiting steps of the CO_2 -to- HCOOH (HCOOH^*) and $-\text{CO}$ (desorption of CO) conversions, suggesting a high activity of H_2O dissociation on S-Cu and its low selectivity of HCOOH during the CO_2RR (Figures 5b and S29; for details of the description, see Figure S29, Supporting Information). Additionally, for the structure of S-Sn, the Gibbs free energy for the formation of OCHO^* is consistent with that on S-CuSn, while the Gibbs free energies of COOH^* and H^* are significantly lower than those on S-CuSn, indicating that the CO_2 -to- CO conversion and HER are more likely to be achieved on S-Sn and thus promoting the production of HCOOH on the

S-CuSn catalyst (Figures 5c and S30; for details of the description, see Figure S30, Supporting Information).

Moreover, the differential charge densities of OCHO^* , regarded as one of the crucial intermediates for the formation of HCOOH , have been calculated for S-CuSn, S-Cu, and S-Sn to further elucidate the mechanism of the interactions between the adsorbate and substrate. As compared to S-Cu and S-Sn, S-CuSn displays that the adsorbed OCHO^* can distinctly induce charge transfer and obvious charge accumulation on the surface of S-CuSn. It further leads to an unbalanced charge distribution at the interphase and strong charge interaction between OCHO^* and S-CuSn, suggesting the high activity of OCHO^* and the enhancement of the formation of HCOOH^* (Figure 5d–f). The charge distribution of the S-CuSn substrate was also investigated. Figure 5g shows the robust charge interactions among the S, Cu, and Sn atoms in S-CuSn, indicating the charge transfer and redistribution at the interfaces between S and CuSn, as well as Sn and CuSn. The 2D contour map was also sliced from the differential charge density distribution, which further demonstrates the unbalanced charge distribution around the S and Sn atoms and the surface of CuSn (Figure 5h). This not only accelerates the charge transfer among S, Cu, and Sn atoms in S-CuSn but also improves the activity of OCHO^* to react with the proton/electron pair or adsorb H^* to further produce HCOOH .^{28,51} Based on the above-mentioned analysis, the possible CO_2RR mechanism on the reconstructed S-CuSn catalyst can be concluded that the doped S and Sn atoms on CuSn alloys enhance the charge transfer to facilitate the reaction with OCHO^* , which can also decrease the energy barrier for the pathway of CO_2 -to- HCOOH conversion on the surface of S-CuSn (Figure 5i). Overall, the results of Gibbs free energy and differential charge density are in good agreement with the experimental observations, further explaining the high selectivity and activity of formate production of the *in situ* constructed S-CuSn catalyst.

3. CONCLUSIONS

In summary, we have thoroughly revealed the *in situ* dynamic reconstruction process of the S-CuSn catalyst under the CO_2RR working conditions. Based on the different characterizations of the precatalyst *in situ* reduced under the working conditions, the overall process can be decoupled into five stages: the reduction of CuS, the leaching of S from Cu_2SnS_3 , the formation of $\text{Cu}_{24}\text{Sn}_{20}$ alloys, the formation of Sn metal, and the stable structure of S/Sn co-doped $\text{Cu}_{24}\text{Sn}_{20}$ alloys. The reconstructed S-CuSn catalyst exhibited excellent catalytic activity for the electrochemical reduction of CO_2 to formate at a wide potential range, achieving a maximum FE of 91.5% with a partial current density (j_{formate}) of about -54.9 mA cm^{-2} (-109.8 A g^{-1}) at -1.20 V vs RHE in a H-cell reactor. Moreover, it also exhibited a maximal FE of 96.4% for formate with a j_{formate} of $-241.0 \text{ mA cm}^{-2}$ (-669.4 A g^{-1}) at -2.22 V vs RHE and an impressive formate production rate of $124889.9 \mu\text{mol mg}^{-1} \text{ h}^{-1}$ in a flow-cell device. Theoretical calculations indicated that the high selectivity and activity of formate production were attributed to the specific electronic structure of S-CuSn and strong charge interactions between the adsorbate and substrate, resulting in the acceleration of the charge transfer and a decrease of the Gibbs free energy for the key intermediates in the pathway of CO_2 to HCOOH . Overall, this work not only demonstrates the reconstruction process and phase transformation of the electrocatalyst under the working conditions, but also provides a new strategy to design electrocatalysts with excellent activity.

■ ASSOCIATED CONTENT

SI Supporting Information

The Supporting Information is available free of charge at <https://pubs.acs.org/doi/10.1021/acscatal.2c02627>.

Details of the experimental and theoretical sections, TEM, HRTEM, H-type, and flow-cell reactor images, details of XPS and XRD, electrochemical data, optimized structures of DFT calculations, free energies, and comparison of the CO₂RR performance (PDF)

■ AUTHOR INFORMATION

Corresponding Authors

Wei Chen – Department of Applied Chemistry, School of Chemistry and Materials Science, Hefei National Research Center for Physical Sciences at the Microscale, University of Science and Technology of China, Hefei, Anhui 230026, P. R. China; orcid.org/0000-0002-8018-4529; Email: weichen1@ustc.edu.cn

Chuan Xia – Yangtze Delta Region Institute (Huzhou), University of Electronic Science and Technology of China, Huzhou 313001, P. R. China; School of Materials and Energy, University of Electronic Science and Technology of China, Chengdu 611731, P. R. China; orcid.org/0000-0003-4526-159X; Email: chuan.xia@uestc.edu.cn

Authors

Ke Li – Department of Applied Chemistry, School of Chemistry and Materials Science, Hefei National Research Center for Physical Sciences at the Microscale, University of Science and Technology of China, Hefei, Anhui 230026, P. R. China

Jingwen Xu – Department of Applied Chemistry, School of Chemistry and Materials Science, Hefei National Research Center for Physical Sciences at the Microscale, University of Science and Technology of China, Hefei, Anhui 230026, P. R. China

Tingting Zheng – Yangtze Delta Region Institute (Huzhou), University of Electronic Science and Technology of China, Huzhou 313001, P. R. China; School of Materials and Energy, University of Electronic Science and Technology of China, Chengdu 611731, P. R. China

Yuan Yuan – Department of Applied Chemistry, School of Chemistry and Materials Science, Hefei National Research Center for Physical Sciences at the Microscale, University of Science and Technology of China, Hefei, Anhui 230026, P. R. China

Shuang Liu – Department of Applied Chemistry, School of Chemistry and Materials Science, Hefei National Research Center for Physical Sciences at the Microscale, University of Science and Technology of China, Hefei, Anhui 230026, P. R. China

Chunyu Shen – Department of Applied Chemistry, School of Chemistry and Materials Science, Hefei National Research Center for Physical Sciences at the Microscale, University of Science and Technology of China, Hefei, Anhui 230026, P. R. China

Taoli Jiang – Department of Applied Chemistry, School of Chemistry and Materials Science, Hefei National Research Center for Physical Sciences at the Microscale, University of Science and Technology of China, Hefei, Anhui 230026, P. R. China

Jifei Sun – Department of Applied Chemistry, School of Chemistry and Materials Science, Hefei National Research

Center for Physical Sciences at the Microscale, University of Science and Technology of China, Hefei, Anhui 230026, P. R. China

Zaichun Liu – Department of Applied Chemistry, School of Chemistry and Materials Science, Hefei National Research Center for Physical Sciences at the Microscale, University of Science and Technology of China, Hefei, Anhui 230026, P. R. China

Yan Xu – Department of Applied Chemistry, School of Chemistry and Materials Science, Hefei National Research Center for Physical Sciences at the Microscale, University of Science and Technology of China, Hefei, Anhui 230026, P. R. China

Mingyan Chuai – Department of Applied Chemistry, School of Chemistry and Materials Science, Hefei National Research Center for Physical Sciences at the Microscale, University of Science and Technology of China, Hefei, Anhui 230026, P. R. China

Complete contact information is available at:

<https://pubs.acs.org/doi/10.1021/acscatal.2c02627>

Author Contributions

The project was conceptualized by K.L. and W.C. and supervised by C. X. and W.C.; K.L. synthesized the catalysts, conducted the electrochemical tests, and performed the theoretical calculations and mechanistic analysis; K.L. conducted the ¹H NMR experiments with the help of J.X.; T.Z., Y.Y., S.L., C.S., T.J., J.S., Z.L., Y.X., M.C., C.X., and W.C. provided suggestions on the work. K.L. and W.C. prepared the article. All authors have given approval to the final version of the article.

Notes

The authors declare no competing financial interest.

■ ACKNOWLEDGMENTS

W.C. acknowledges the startup funds from USTC (Grant # KY2060000150) and the Fundamental Research Funds for the Central Universities (Grant # WK2060000040). C.X. acknowledges the National Natural Science Foundation of China (NSFC 22102018 and 52171201), the Natural Science Foundation of Sichuan Province (2022NSFSC0194), the Central Government Funds of Guiding Local Scientific and Technological Development for Sichuan Province (no. 2021ZYD0043), the University of Electronic Science and Technology of China for startup funding (A1098531023601264), and the Hefei National Research Center for Physical Sciences at the Microscale (KF2021005). K.L. acknowledges the National Natural Science Foundation of China (Grant No. 52102191) and the advanced computing resources provided by the Supercomputing Center of the USTC. This work was also supported by the USTC Center for Micro- and Nanoscale Research.

■ REFERENCES

- (1) Luna, P. D.; Hahn, C.; Higgins, D.; Jaffer, S. A.; Jaramillo, T. F.; Sargent, E. H. What would it take for renewably powered electrosynthesis to displace petrochemical processes? *Science* **2019**, *364*, No. eaav3506.
- (2) Bushuyev, O. S.; Luna, P. D.; Dinh, C. T.; Tao, L.; Saur, G.; Lagemaat, J. vd.; Kelley, S. O.; Sargent, E. H. What should we make with CO₂ and how can we make it? *Joule* **2018**, *2*, 825–832.
- (3) Chu, S.; Cui, Y.; Liu, N. The path towards sustainable energy. *Nat. Mater.* **2017**, *16*, 16–22.

- (4) Xia, C.; Zhu, P.; Jiang, Q.; Pan, Y.; Liang, W.; Stavitski, E.; Alshareef, H. N.; Wang, H. Continuous production of pure liquid fuel solutions via electrocatalytic CO₂ reduction using solid-electrolyte devices. *Nat. Energy* **2019**, *4*, 776–785.
- (5) Zheng, T.; Liu, C.; Guo, C.; Zhang, M.; Li, X.; Jiang, Q.; Xue, W.; Li, H.; Li, A.; Pao, C.-W.; Xiao, J.; Xia, C.; Zeng, J. Copper-catalysed exclusive CO₂ to pure formic acid conversion via single-atom alloying. *Nat. Nanotechnol.* **2021**, *16*, 1386–1393.
- (6) Chen, M.; Wan, S.; Zhong, L.; Liu, D.; Yang, H.; Li, C.; Huang, Z.; Liu, C.; Chen, J.; Pan, H.; Li, D. S.; Li, S.; Yan, Q.; Liu, B. Dynamic restructuring of Cu-doped SnS₂ nanoflowers for highly selective electrochemical CO₂ reduction to formate. *Angew. Chem., Int. Ed.* **2021**, *60*, 26233–26237.
- (7) Chi, L.-P.; Niu, Z.-Z.; Zhang, X.-L.; Yang, P.-P.; Liao, J.; Gao, F.-Y.; Wu, Z.-Z.; Tang, K.-B.; Gao, M.-R. Stabilizing indium sulfide for CO₂ electroreduction to formate at high rate by zinc incorporation. *Nat. Commun.* **2021**, *12*, No. 5835.
- (8) Feaster, J. T.; Shi, C.; Cave, E. R.; Hatsukade, T.; Abram, D. N.; Kuhl, K. P.; Hahn, C.; Nørskov, J. K.; Jaramillo, T. F. Understanding selectivity for the electrochemical reduction of carbon dioxide to formic acid and carbon monoxide on metal electrodes. *ACS Catal.* **2017**, *7*, 4822–4827.
- (9) Fan, L.; Xia, C.; Zhu, P.; Lu, Y.; Wang, H. Electrochemical CO₂ reduction to high-concentration pure formic acid solutions in an all-solid-state reactor. *Nat. Commun.* **2020**, *11*, No. 3633.
- (10) Liu, C.; Zhang, M.; Li, J.; Xue, W.; Zheng, T.; Xia, C.; Zeng, J. Nanoconfinement engineering over hollow multi-shell structured copper towards efficient electrocatalytic C–C coupling. *Angew. Chem., Int. Ed.* **2022**, *61*, No. e202113498.
- (11) Yang, H. B.; Hung, S.-F.; Liu, S.; Yuan, K.; Miao, S.; Zhang, L.; Huang, X.; Wang, H.-Y.; Cai, W.; Chen, R.; Gao, J.; Yang, X.; Chen, W.; Huang, Y.; Chen, H. M.; Li, C. M.; Zhang, T.; Liu, B. Atomically dispersed Ni(i) as the active site for electrochemical CO₂ reduction. *Nat. Energy* **2018**, *3*, 140–147.
- (12) Choi, C.; Cai, J.; Lee, C.; Lee, H. M.; Xu, M.; Huang, Y. Intimate atomic Cu–Ag interfaces for high CO₂RR selectivity towards CH₄ at low over potential. *Nano Res.* **2021**, *14*, 3497–3501.
- (13) Zhu, Z. H.; Zhao, B. H.; Hou, S. L.; Jiang, X. L.; Liang, Z. L.; Zhang, B.; Zhao, B. A facile strategy for constructing a carbon-particle-modified metal–organic framework for enhancing the efficiency of CO₂ electroreduction into formate. *Angew. Chem., Int. Ed.* **2021**, *60*, 23394–23402.
- (14) Kim, J.-Y.; Hong, D.; Lee, J.-C.; Kim, H. G.; Lee, S.; Shin, S.; Kim, B.; Lee, H.; Kim, M.; Oh, J.; Lee, G.-D.; Nam, D.-H.; Joo, Y.-C. Quasi-graphitic carbon shell-induced Cu confinement promotes electrocatalytic CO₂ reduction toward C₂₊ products. *Nat. Commun.* **2021**, *12*, No. 3765.
- (15) Xu, H.; Rebollar, D.; He, H.; Chong, L.; Liu, Y.; Liu, C.; Sun, C.-J.; Li, T.; Muntean, J. V.; Winans, R. E.; Liu, D.-J.; Xu, T. Highly selective electrocatalytic CO₂ reduction to ethanol by metallic clusters dynamically formed from atomically dispersed copper. *Nat. Energy* **2020**, *5*, 623–632.
- (16) Peng, C.; Luo, G.; Zhang, J.; Chen, M.; Wang, Z.; Sham, T.-K.; Zhang, L.; Li, Y.; Zheng, G. Double sulfur vacancies by lithium tuning enhance CO₂ electroreduction to n-propanol. *Nat. Commun.* **2021**, *12*, No. 1580.
- (17) Eppinger, J.; Huang, K.-W. Formic acid as a hydrogen energy carrier. *ACS Energy Lett.* **2017**, *2*, 188–195.
- (18) Grigioni, L.; Sagar, L. K.; Li, Y. C.; Lee, G.; Yan, Y.; Bertens, K.; Miao, R. K.; Wang, X.; Abed, J.; Won, D. H.; Arquer, F. P. G. ad.; Ip, A. H.; Sinton, D.; Sargent, E. H. CO₂ electroreduction to formate at a partial current density of 930 mA cm^{−2} with InP colloidal quantum dot derived catalysts. *ACS Energy Lett.* **2021**, *6*, 79–84.
- (19) Yang, Q.; Wu, Q.; Liu, Y.; Luo, S.; Wu, X.; Zhao, X.; Zou, H.; Long, B.; Chen, W.; Liao, Y.; Li, L.; Shen, P. K.; Duan, L.; Quan, Z. Novel bi-doped amorphous SnO_x nanoshells for efficient electrochemical CO₂ reduction into formate at low overpotentials. *Adv. Mater.* **2020**, *32*, No. 2070392.
- (20) Duan, Y. X.; Zhou, Y. T.; Yu, Z.; Liu, D. X.; Wen, Z.; Yan, J. M.; Jiang, Q. Boosting production of HCOOH from CO₂ electroreduction via Bi/CeO_x. *Angew. Chem., Int. Ed.* **2021**, *60*, 8798–8802.
- (21) Pérez, L. C. P.; Teschner, D.; Willinger, E.; Guet, A.; Driess, M.; Strasser, P.; Fischer, A. In situ formed “Sn_{1−x}In_x@In_{1−y}Sn_yO_z” core@shell nanoparticles as electrocatalysts for CO₂ reduction to formate. *Adv. Funct. Mater.* **2021**, *31*, No. 2103601.
- (22) Ye, K.; Zhou, Z.; Shao, J.; Lin, L.; Gao, D.; Ta, N.; Si, R.; Wang, G.; Bao, X. In situ reconstruction of a hierarchical Sn–Cu/SnO_x core/shell catalyst for high-performance CO₂ electroreduction. *Angew. Chem., Int. Ed.* **2020**, *59*, 4814–4821.
- (23) Wen, G.; Lee, D. U.; Ren, B.; Hassan, F. M.; Jiang, G.; Cano, Z. P.; Gostick, J.; Croiset, E.; Bai, Z.; Yang, L.; Chen, Z. Orbital interactions in Bi–Sn bimetallic electrocatalysts for highly selective electrochemical CO₂ reduction toward formate production. *Adv. Energy Mater.* **2018**, *8*, No. 1802427.
- (24) Cheng, F.; Zhang, X.; Mu, K.; Ma, X.; Jiao, M.; Wang, Z.; Limpachanangkul, P.; Chalermisinsuwan, B.; Gao, Y.; Li, Y.; Chen, Z.; Liu, L. Recent progress of Sn-based derivative catalysts for electrochemical reduction of CO₂. *Energy Technol.* **2021**, *9*, No. 2000799.
- (25) Ye, K.; Cao, A.; Shao, J.; Wang, G.; Si, R.; Ta, N.; Xiao, J.; Wang, G. Synergy effects on Sn–Cu alloy catalyst for efficient CO₂ electroreduction to formate with high mass activity. *Sci. Bull.* **2020**, *65*, 711–719.
- (26) Yan, S.; Peng, C.; Yang, C.; Chen, Y.; Zhang, J.; Guan, A.; Lv, X.; Wang, H.; Wang, Z.; Sham, T. K.; Han, Q.; Zheng, G. Electron localization and lattice strain induced by surface lithium doping enable amper-level electrosynthesis of formate from CO₂. *Angew. Chem., Int. Ed.* **2021**, *133*, 25945–25949.
- (27) Ren, M.; Zheng, H.; Lei, J.; Zhang, J.; Wang, X.; Jakobson, B. I.; Yao, Y.; Tour, J. M. CO₂ to formic acid using Cu–Sn on laser-induced graphene. *ACS Appl. Mater. Interfaces* **2020**, *12*, 41223–41229.
- (28) Ma, W.; Xie, S.; Zhang, X.-G.; Sun, F.; Kang, J.; Jiang, Z.; Zhang, Q.; Wu, D.-Y.; Wang, Y. Promoting electrocatalytic CO₂ reduction to formate via sulfur-boosting water activation on indium surfaces. *Nat. Commun.* **2019**, *10*, No. 892.
- (29) Zou, J.; Lee, C. Y.; Wallace, G. G. Boosting formate production from CO₂ at high current densities over a wide electrochemical potential window on a SnS catalyst. *Adv. Sci.* **2021**, *8*, No. 2004521.
- (30) Zheng, X.; Luna, P. D.; Arquer, F. P. G. d.; Zhang, B.; Becknell, N.; Ross, M. B.; Li, Y.; Banis, M. N.; Li, Y.; Liu, M.; Voznyy, O.; Dinh, C. T.; Zhuang, T.; Stadler, P.; Cui, Y.; Du, X.; Yang, P.; Sargent, E. H. Sulfur-modulated tin sites enable highly selective electrochemical reduction of CO₂ to formate. *Joule* **2017**, *1*, 794–805.
- (31) Zhou, X.; Shan, J.; Chen, L.; Xia, B. Y.; Ling, T.; Duan, J.; Jiao, Y.; Zheng, Y.; Qiao, S.-Z. Stabilizing Cu²⁺ ions by solid solutions to promote CO₂ electroreduction to methane. *J. Am. Chem. Soc.* **2022**, *144*, 2079–2084.
- (32) Zhou, X.; Dong, J.; Zhu, Y.; Liu, L.; Jiao, Y.; Li, H.; Han, Y.; Davey, K.; Xu, Q.; Zheng, Y.; Qiao, S.-Z. Molecular scalpel to chemically cleave metal–organic frameworks for induced phase transition. *J. Am. Chem. Soc.* **2021**, *143*, 6681–6690.
- (33) Vasileff, A.; Zhu, Y.; Zhi, X.; Zhao, Y.; Ge, L.; Chen, H. M.; Zheng, Y.; Qiao, S.-Z. Electrochemical reduction of CO₂ to ethane through stabilization of an ethoxy intermediate. *Angew. Chem., Int. Ed.* **2020**, *59*, 19649–19653.
- (34) Wang, W.; Wang, Z.; Yang, R.; Duan, J.; Liu, Y.; Nie, A.; Li, H.; Xia, B. Y.; Zhai, T. In situ phase separation into coupled interfaces for promoting CO₂ electroreduction to formate over a wide potential window. *Angew. Chem., Int. Ed.* **2021**, *133*, 23122–23129.
- (35) Yao, D.; Tang, C.; Vasileff, A.; Zhi, X.; Jiao, Y.; Qiao, S. Z. The controllable reconstruction of Bi–MOFs for electrochemical CO₂ reduction through electrolyte and potential mediation. *Angew. Chem., Int. Ed.* **2021**, *60*, 18178–18184.
- (36) Chalapati, U.; Poornaprakash, B.; Park, S.-H. Antimony induced crystal growth for large-grained Cu₂SnS₃ thin films for photovoltaics. *J. Power Sources* **2019**, *426*, 84–92.

- (37) Naille, S.; Dedryvère, R.; Martinez, H.; Leroy, S.; Lippens, P. E.; Jumas, J. C.; Gonbeau, D. XPS study of electrode/electrolyte interfaces of η -Cu₆Sn₅ electrodes in Li-ion batteries. *J. Power Sources* **2007**, *174*, 1086–1090.
- (38) Wang, W.; Wang, Z.; Yang, R.; Duan, J.; Liu, Y.; Nie, A.; Li, H.; Xia, B. Y.; Zhai, T. In situ phase separation into coupled interfaces for promoting CO₂ electroreduction to formate over a wide potential window. *Angew. Chem., Int. Ed.* **2021**, *133*, 23122–23129.
- (39) Jiang, T.; Li, K.; Park, S.; Zheng, K.; Meng, Y.; Yuan, Y.; Liu, Z.; Zhu, Z.; Zheng, X.; Liu, S.; Chen, W. Facile fabrication of bifunctional hydrogen catalytic electrodes for long-life nickel–hydrogen gas batteries. *Nano Lett.* **2022**, *22*, 1741–1749.
- (40) Wang, X.; Lv, J.; Zhang, J.; Wang, X.-L.; Xue, C.; Bian, G.; Li, D.; Wang, Y.; Wu, T. Hierarchical heterostructure of SnO₂ confined on CuS nanosheets for efficient electrocatalytic CO₂ reduction. *Nanoscale* **2020**, *12*, 772–784.
- (41) Xiong, W.; Yang, J.; Shuai, L.; Hou, Y.; Qiu, M.; Li, X.; Leung, M. K. H. CuSn alloy nanoparticles on nitrogen-doped graphene for electrocatalytic CO₂ reduction. *ChemElectroChem* **2019**, *6*, 5951–5957.
- (42) Liu, J.; Li, Y.; Wang, Y.; Xiao, C.; Liu, M.; Zhou, X.; Jiang, H.; Li, C. Isolated ultrasmall Bi nanosheets for efficient CO₂-to-formate electroreduction. *Nano Res.* **2022**, *15*, 1409–1414.
- (43) Wu, Z.; Zhao, Y.; Jin, W.; Jia, B.; Wang, J.; Ma, T. Recent progress of vacancy engineering for electrochemical energy conversion related applications. *Adv. Funct. Mater.* **2021**, *31*, No. 2009070.
- (44) Qin, B.; Li, Y.; Wang, H.; Yang, G.; Cao, Y.; Yu, H.; Zhang, Q.; Liang, H.; Peng, F. Efficient electrochemical reduction of CO₂ into CO promoted by sulfur vacancies. *Nano Energy* **2019**, *60*, 43–51.
- (45) Li, P.; Fu, W.; Zhuang, P.; Cao, Y.; Tang, C.; Watson, A. B.; Dong, P.; Shen, J.; Ye, M. Amorphous Sn/crystalline SnS₂ nanosheets via in situ electrochemical reduction methodology for highly efficient ambient N₂ fixation. *Small* **2019**, *15*, No. 1902535.
- (46) Han, N.; Sun, M.; Zhou, Y.; Xu, J.; Cheng, C.; Zhou, R.; Zhang, L.; Luo, J.; Huang, B.; Li, Y. Alloyed palladium–silver nanowires enabling ultrastable carbon dioxide reduction to formate. *Adv. Mater.* **2021**, *33*, No. 2005821.
- (47) Huang, Y.; Mao, X.; Yuan, G.; Zhang, D.; Pan, B.; Deng, J.; Shi, Y.; Han, N.; Li, C.; Zhang, L.; Wang, L.; He, L.; Li, Y.; Li, Y. Size-dependent selectivity of electrochemical CO₂ reduction on converted In₂O₃ nanocrystals. *Angew. Chem.* **2021**, *133*, 15978–15982.
- (48) Li, Z.; Cao, A.; Zheng, Q.; Fu, Y.; Wang, T.; Arul, K. T.; Chen, J. L.; Yang, B.; Adli, N. M.; Lei, L.; Dong, C. L.; Xiao, J.; Wu, G.; Hou, Y. Elucidation of the synergistic effect of dopants and vacancies on promoted selectivity for CO₂ electroreduction to formate. *Adv. Mater.* **2021**, *33*, No. 2005113.
- (49) Ma, W.; Bu, J.; Liu, Z.; Yan, C.; Yao, Y.; Chang, N.; Zhang, H.; Wang, T.; Zhang, J. Monoclinic scheelite bismuth vanadate derived bismuthene nanosheets with rapid kinetics for electrochemically reducing carbon dioxide to formate. *Adv. Funct. Mater.* **2021**, *31*, No. 2006704.
- (50) Cao, C.; Ma, D. D.; Gu, J. F.; Xie, X.; Zeng, G.; Li, X.; Han, S. G.; Zhu, Q. L.; Wu, X. T.; Xu, Q. Metal–organic layers leading to atomically thin bismuthene for efficient carbon dioxide electroreduction to liquid fuel. *Angew. Chem.* **2020**, *132*, 15124–15130.
- (51) Yang, F.; Elnabawy, A. O.; Schimmenti, R.; Song, P.; Wang, J.; Peng, Z.; Yao, S.; Deng, R.; Song, S.; Lin, Y.; Mavrikakis, M.; Xu, W. Bismuthene for highly efficient carbon dioxide electroreduction reaction. *Nat. Commun.* **2020**, *11*, No. 1088.
- (52) Shi, Y.; Ji, Y.; Long, J.; Liang, Y.; Liu, Y.; Yu, Y.; Xiao, J.; Zhang, B. Unveiling hydrocerussite as an electrochemically stable active phase for efficient carbon dioxide electroreduction to formate. *Nat. Commun.* **2020**, *11*, No. 3415.
- (53) Zeng, Z.; Gan, L. Y.; Yang, H. B.; Su, X.; Gao, J.; Liu, W.; Matsumoto, H.; Gong, J.; Zhang, J.; Cai, W.; Zhang, Z.; Yan, Y.; Liu, B.; Chen, P. Orbital coupling of hetero-diatom nickel-iron site for bifunctional electrocatalysis of CO₂ reduction and oxygen evolution. *Nat. Commun.* **2021**, *12*, No. 4088.
- (54) Kortlever, R.; Shen, J.; Schouten, K. J. P.; Calle-Vallejo, F.; Koper, M. T. M. Catalysts and reaction pathways for the electrochemical reduction of carbon dioxide. *J. Phys. Chem. Lett.* **2015**, *6*, 4073–4082.
- (55) Li, K.; Zhang, S.; Zhang, X.; Liu, S.; Jiang, H.; Jiang, T.; Shen, C.; Yu, Y.; Chen, W. Atomic tuning of single-atom Fe–N–C catalysts with phosphorus for robust electrochemical CO₂ reduction. *Nano Lett.* **2022**, *22*, 1557–1565.
- (56) Staszak-Jirkovský, J.; Malliakas, C. D.; Lopes, P. P.; Danilovic, N.; Kota, S. S.; Chang, K.-C.; Genorio, B.; Strmcnik, D.; Stamenkovic, V. R.; Kanatzidis, M. G.; Markovic, N. M. Design of active and stable Co–Mo–S_x chalcogenes as pH-universal catalysts for the hydrogen evolution reaction. *Nat. Mater.* **2016**, *15*, 197–203.

Recommended by ACS

Spontaneously Formed CuS_x Catalysts for Selective and Stable Electrochemical Reduction of Industrial CO₂ Gas to Formate

Jin Wook Lim, Jong-Lam Lee, *et al.*

MAY 11, 2020

ACS APPLIED MATERIALS & INTERFACES

READ

Selective Enhancement of Methane Formation in Electrochemical CO₂ Reduction Enabled by a Raman-Inactive Oxygen-Containing Species on Cu

Ming He, Qi Lu, *et al.*

MAY 06, 2022

ACS CATALYSIS

READ

Revealing the Surface Chemistry for CO₂ Hydrogenation on Cu/CeO_{2-x} Using Near-Ambient-Pressure X-ray Photoelectron Spectroscopy

Mo Li, Andreas Züttel, *et al.*

OCTOBER 12, 2021

ACS APPLIED ENERGY MATERIALS

READ

Stable Surface-Anchored Cu Nanocubes for CO₂ Electroreduction to Ethylene

Siyu Kuang, Sheng Zhang, *et al.*

JULY 27, 2020

ACS APPLIED NANO MATERIALS

READ

Get More Suggestions >